La-doped SnO$_2$ as ETL for efficient planar-structure hybrid perovskite solar cells

Zhenhua Xu,[a] Siow Hwa Teo,[a] Liguo Gao,[b] Zhanglin Guo,[a] Yusuke Kamata,[a] Shuzi Hayase,[a] and Tingli Ma *[a]

[a] Graduate School of Life Science and Systems Engineering, Kyushu Institute of Technology, Kitakyushu, Fukuoka 808-0196, Japan.

E-mail:tinglima@life.kyutech.ac.jp

[b] School of Petroleum and Chemical Engineering, Dalian University of Technology, Panjin Campus, Panjin 124221, P. R. China

Abstract

SnO$_2$ has attracted considerable attention in perovskite solar cells (PSCs) due to its excellent optical and electrical properties. However, a poor surface morphology, specifically with the presence of pinholes after the annealing process, limits its application in PSCs. To overcome the drawback of tin oxide, lanthanum (La) is herein first to be doped into the SnO$_2$ layer, which is able to alleviate the SnO$_2$ crystal aggregation and produce full-coverage and a uniform film. In addition, La:SnO$_2$ can effectively reduce the band offset of the SnO$_2$ layer, which results in the high Voc of 1.11 V. Systematic analyses revealed that the La:SnO$_2$ layer enhances the electron extraction and suppresses charge recombination, leading to the power conversion efficiency (PCE) enhancement from 14.24% to 17.08%.

KEYWORDS: Lanthanide doping, SnO$_2$ electron transport layer, perovskite solar cells, high conductivity.

1. Introduction

PSCs have experienced rapid progress since an organic-inorganic hybrid $CH_3NH_3PbI_3$ perovskite was first introduced as a light absorber in 2009 [1]. The organic-inorganic hybrid perovskite ($APbX_3$, A = CH_3NH_3, $CH(NH_2)_2$, or Cs; X = I^-, Br^- or Cl^-), in which the organic group stabilizes the $(PbX_6)^-$ octahedron structure, have witnessed a dramatic development in solar cells [2]. The PCE has risen to 23.1% for a PSC which employed TiO_2 as the electron transport layer (ETL) [3-5]. However, the traditional TiO_2 as an ETL is inefficient for charge extraction at the perovskite/TiO_2 interface. In addition, the devices using TiO_2 suffer from serious degradation under ultraviolet light, thus its stability limits its further application. SnO_2 is a highly conductive n-type semiconductor in nature and quite stable for solar radiation. In addition, SnO_2 with an electron mobility of 1×10^{-3} $cm^2V^{-1}s^{-1}$ is higher than that of TiO_2 of ca. 1×10^{-4} $cm^2V^{-1}s^{-1}$, which suppresses charges accumulation at the SnO_2/perovskite interface [6-10]. SnO_2 is easily synthesized at low temperature, showing the potential for PSCs in large-scale applications [11-13]. To date, You et al. achieved the champion PCE of 23.23% for perovskite solar cells based on the SnO_2 ETL [14]. Therefore, SnO_2 is a very promising ETL material for highly efficient PSCs.

However, a SnO_2-based ETL with spontaneous aggregation results in pinholes or island morphology. The poor film performance hinders photo-generated electron injection into the SnO_2 electron acceptor. To solve this issue, several solutions have been attempted to reduce the SnO_2 defects, such as surface passivation, i.e., PCBM, n-type metallic oxide, graphene quantum dots [15-27], have proven its effectiveness in reducing the surface defects and surface electron traps of SnO_2 to improve the efficiency [28-29]. Another important strategy is ion doping to change the band structure and trap states of the SnO_2. Alkali metallic ions, such as Li^+, K^+, Mg^{2+}, and Al^{3+}, are expected to improve the conductivity and stability of the SnO_2 layer. The

superior conductivity of the alkali ions is able to reduce the series resistance, consequently improving the open-circuit voltage (Voc) [30-32]. Other dopants, such as the n-type Cd^{3+}, Sb^{3+}, Y^{3+}, and Nb^{5+}, are purposed to create donor centers to accelerate the charge mobility and to alleviate the photo-generated electron accumulation, for enhancements of the short-circuit density (Jsc) and fill factor (FF) [33-35]. In addition, F^- and Cl^- anion dopants have also been discussed. The researchers found that the conductivity of anion-doped SnO_2 is increased, along with the reduced band offset, resulting in an increased Voc [36-39].

On the other hand, the rare earth element is a good doping candidate due to its unique optical and electronic properties from its unfilled 4f electronic shell. When it is incorporated into the ETLs, lanthanide could have an impact on the ETL optical property and stability. Seok group employed La-doped $BaSnO_3$ as efficient ETL for the PSCs. Lanthanide in the $BaSnO_3$ crystal exhibited a high electrical mobility of 320 $cm^2 \cdot V^{-1} \cdot s^{-1}$, promoted the electron extraction from the perovskite layer, and showed a superior steady-state PCE of 21.2% [40]. Gao and his coworker tuned the TiO_2 ETL Fermi level by doping La^{3+} into mesoporous TiO_2, thus achieving a PCE of 15.42% [41]. Due to the inherent properties of the lanthanide, it exerts beneficial effects on the SnO_2 ETL [42].

In this direction, we first employed the lanthanide doped SnO_2 compact layer for planar PSCs, with the PCE achievement of 17.08%. After doping the lanthanide, the morphology of the SnO_2 layer was obviously improved. Lanthanide doping affects the crystallization of SnO_2 during the annealing process, where perfect film coverage was obtained without crystal aggregation and pinholes. In addition, lanthanide doping improved the conductivity of the SnO_2 layer and upward shift of the conductive band minimum (CBM), which contributed to the Voc increase and suppressed the hysteresis behavior. Our simple interfacial control approach uses a

new efficient dopant material, demonstrating that lanthanide doping can be a feasible strategy for improving the performance of perovskite solar cells.

2. Experimental

2.1. Materials

Ethanol, diethyl ether, anhydrous dimethylformamide (DMF) (99.8%), anhydrous dimethylsulfoxide (DMSO) (99.9%), anhydrous ethanol, anhydrous diethyl ether (99.9%), lanthanide chloride (LaCl$_3$·5H$_2$O, 99.8%) and anhydrous tin chloride (SnCl$_2$, 99.95%) were purchased from Wako, Japan. PbI$_2$ and methylammonium iodine (MAI) was purchased from Deysol. Spiro-OMeTAD was purchased from the Ningbo Borun New Material Corporation. 4-Tert-butylpyridine (t-BP), and Li-bis-(trifluoromethanesulfonyl) imide (Li-TFSI) were purchased from Alfa-Aesar. All solvents were used without any further purification

2.2. Compact La:SnO$_2$ layer fabrication

Fluorine-doped tin oxide (FTO) glass was chemically etched (Zn powder and 2 M HCl) to attain a partial etching pattern with a width of roughly 5 mm. The etched FTO substrate was then cleaned with a surfactant and successively rinsed with acetone, ethanol and deionized water and finally dried in an oven. 0.189 g SnCl$_2$ was dissolved in 10 mL of absolute ethyl alcohol (0.1mol/L) with an extra 36 μL of deionized water. For the lanthanide doping precursors, lanthanide (III) chloride was dissolved in absolute ethyl alcohol to form a solution with a 0.8 mol/L concentration. Different dosage, 1μL, 2.5 μL, and 5 μL LaCl$_3$ solution were added to the 1 mL tin precursor to obtain 1%, 2.5%, and 5% molar ratio doped samples, respectively. All the precursor solutions were filtered through a 0.22 μm PTFE filter before use. The precursors were spin coated on a clean FTO glass at 2000 rpm for 30s, then annealed at 100 °C for 10 min and at 180°C for 1 h.

2.3. Perovskite solar cell device fabrication

A device with an n-i-p regular planar structure of FTO/SnO$_2$/MAPbI$_3$/Spiro-OMeTAD/Au was fabricated in a N$_2$-filled glove box. The precursor solution of the one-step perovskite deposition was prepared by dissolving 0.22g methylammonium iodide (CH$_3$NH$_3$I) and 0.64 g lead iodide (PbI$_2$) in a solution of 800 μL DMF and 200 μL DMSO (4:1, v:v), then stirred for 2 hours at 60 °C. The HTL solution was prepared by dissolving 72.3 mg of spiro-OMeTAD, 28.8 μL of 4-tert-butylpyridine, and 17.5 μL of lithium bis-(trifluoromethanesulfonyl) imide (Li-TFSI) (520 mg Li-TFSI in 1 mL acetonitrile) in 1 mL of chlorobenzene. All solutions were filtered through a PTFE filter (0.2 μm pore size) before use. After the SnO$_2$ or La:SnO$_2$ layer was treated by UV-Ozone for 15 min, the MAPbI$_3$ precursor was spin-coated at 4000 rpm for 30 s. A 150 μL of ethyl acetate was dropped on top of the perovskite precursor 20s before the end. Afterward, the perovskite layer was sintered at 100 °C for 10 min. A 75 μL of spiro-OMeTAD was spin coated at 4000 rpm for 30s. Before the device was tested, 80 nm Au was thermally evaporated on the device at a ratio of 0.5 Å/s.

2.4. Characteristics

The X-ray diffraction (XRD) was scanned from 5 ° to 80 ° at the rate of 0.01°s^{-1} using an X-ray diffractometer (Rigaku Co., Ltd., Tokyo, Japan) with Cu Kα radiation (λ=1. 54056 Å). The field emission scanning electron microscope (FE-SEM) (JSM-6701, JEOL) was used to capture the morphology of the perovskite films. A UV-VIS-NIR spectrophotometer (V-670, JASCO Co., Ltd., USA) was measured to characterize the optical properties of the samples. The Fourier transform infrared spectroscopy (FTIR) was carried out using a spectrometer (4100, Jasco Instruments, USA). The IPCE was applied to record the perovskite absorption by monochromatic illumination (A 300 W Xenon arc lamp through a Nikon G250 monochromator).

The transient photovoltage decay measurements were carried out using a 630-nm diode laser via the 5ns pulse duration and frequency of 4 Hz. The voltage responses from the device were recorded using a DS-5554 Iwatsu digital oscilloscope. The electrochemical impedance spectroscopy (EIS) was carried out by the 1255B Solartron Analytical. The current response to voltage (J-V) curve was measured by a Keithley 2450 solar simulator interfaced with a Xenon lamp (Bunko Keiki BSOX150LC) at 100 mW cm^{-2} under AM 1.5G conditions. The cell area was controlled at 0.08 cm^2 by a black metal mask to measure the photovoltaic performance of the devices. The valence band of the SnO_2 films was measured using photoelectron yield spectroscopy (KV205-HK energy instrument, Japan). When the SnO_2 layer is activated by the certain incident light, the photoelectron current is detected by the sensor. The output data are photo energy (Eg) and yield of photoelectrons (Yield). The resolution of PYS was 0.01 eV.

3. Results and discussion

3.1. Characterization of La:SnO_2 layer and La:SnO_2-based PSCs device

FTIR was first employed to study the effect of lanthanide on the tin solution precursor. As shown in Figure 1a, the peaks at around 3340 cm^{-1}, 2979 cm^{-1}, 1039 cm^{-1} represent O-H, C-H, and C-O stretching vibrations of ethanol, respectively. The peaks at 1380 cm^{-1} and 878 cm^{-1} are attributed to the C-H bending vibration. It should be noted that peak at 3670 cm^{-1} is attributed to the tin-induced O-H stretching vibration, which is commonly observed in a ligand complex solution. In addition, the peak is sharper after lanthanide doping of the precursor. The characteristic peaks of the lanthanide ethanol solution are located at 2357 cm^{-1} and 1735 cm^{-1}. Similar peaks are also observed for the lanthanide-doped precursor, indicating a small amount of lanthanide doping into the precursor lead to a chemical atmosphere change. Therefore, lanthanide doping affects the crystallization of SnO_2 during the

annealing process. The influence of dopants on the precursor are universal but rarely mentioned, and the mechanism could be explained by the Debye-Hückel equation (Equation S1). La^{3+} dopant enhances the stability of tin ligand compound in solution, wherein it prevents the small tin ethanol complex from aggregating during the sintering process.
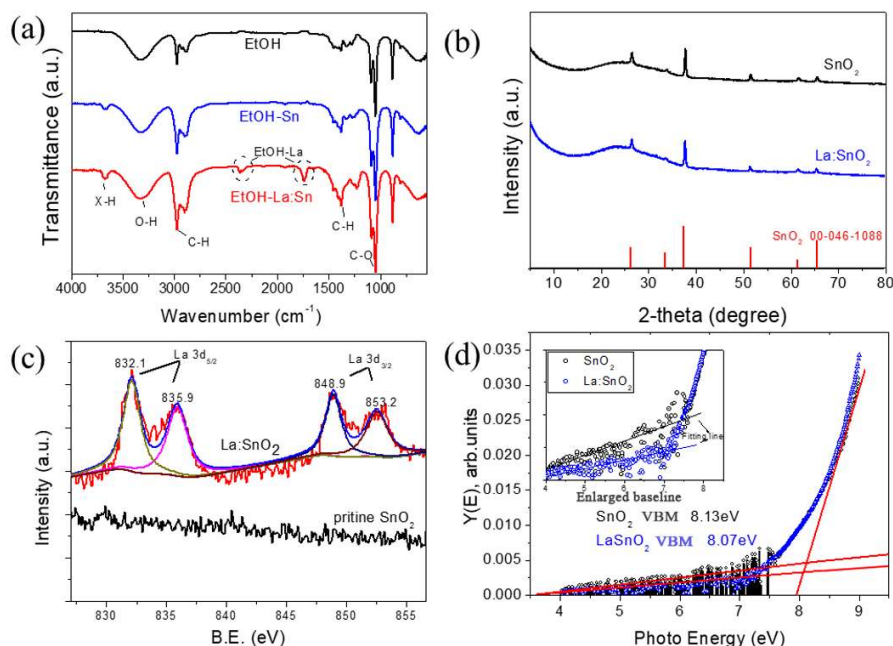

Figure 1. (a) The Fourier transform infrared spectroscopy (FTIR) of tin and La-doped tin precursors in ethanol solution. (b) XRD pattern of SnO$_2$ and La:SnO$_2$ (2.5% molar ratio) deposited on FTO substrate. (c) XPS surveys of La 3d pattern on La:SnO$_2$ and SnO$_2$ layers. (d) Photoelectron yield spectroscopy (PYS) spectrum of SnO$_2$ and La:SnO$_2$ layers, respectively.

After the precursor is spin coated on the FTO substrate, the corresponding X-ray diffraction (XRD) spectrum is presented in Figure 1b. The main peaks located at 26.33°, 37.80°, 51.47° are indexed to (110), (101), and (211) respectively, indicative of a tetragonal rutile SnO$_2$ structure, and importantly, the lanthanide dopant does not

induce disruption [40]. In addition, the XRD peaks of SnO_2 with or without the La dopant are identical, indicating that the lanthanide dopant is homogeneously dispersed in the SnO_2 crystal. Figure 1c displays the XPS pattern of La:SnO_2 where the SnO_2 layer with 2.5% lanthanide doping exhibits four peaks with binding energies of 832.1 eV, 835.9 eV, 848.9 eV, and 853.2 eV, which correspond to La $3d_{5/2}$ and La $3d_{3/2}$, thus proving the existence of La^{3+}. The wide spectrum of XPS and Sn 3d is showed in Fig. S1, the Sn 3d have no obvious changed after La doping. The valence band maximum (VBM) of the La:SnO_2 and SnO_2 layers were determined by photoelectron yield spectroscopy (PYS). As Figure 1d revealed, the VBM edge is determined from the intersection point between the tangent line and the baseline of the spectra. Subsequently, by combining the results of the band gap energy ($E_{bandgap}$) and VBM, the conduction band minimum (CBM) is determined, as depicted in Figure S2. The shallower CBM increase (shifted from -4.09 eV to -4.02 eV) thus increases the Voc of the PSCs.

The conductivity of the SnO_2 before and after the addition of the lanthanide was investigated by a bias voltage sweep under the light condition, as illustrated in Figure 2a. The electrical conductivity of the pristine SnO_2 recorded a value of 50 $\Omega \cdot cm^{-2}$ and it increases along with the change in the lanthanide to 30$\Omega \cdot cm^{-2}$, which is consistent with the conductivity value reported in the literature (30 $\Omega \cdot cm^{-2}$) [43]. Figure 2 shows the optical transmission spectra of SnO_2 from the wavelength of 300 nm to 800 nm. The transparency increase after the lanthanide doping indicates that the La^{3+} is beneficial for the SnO_2 optical transmittance performance. La:SnO_2 samples with a high transparency and conductivity enhance the electron transport. Also, the addition of La within the SnO_2 framework shifted the CBM closer to the perovskite layer (-4.02 eV), hence, an ease transport of electrons to the ETL layer. Figure 2d displays a cross-sectional SEM image of the complete device. The

perovskite crystal is in close contact with the compact La:SnO$_2$ layer, which benefits the longitudinal carrier transport.
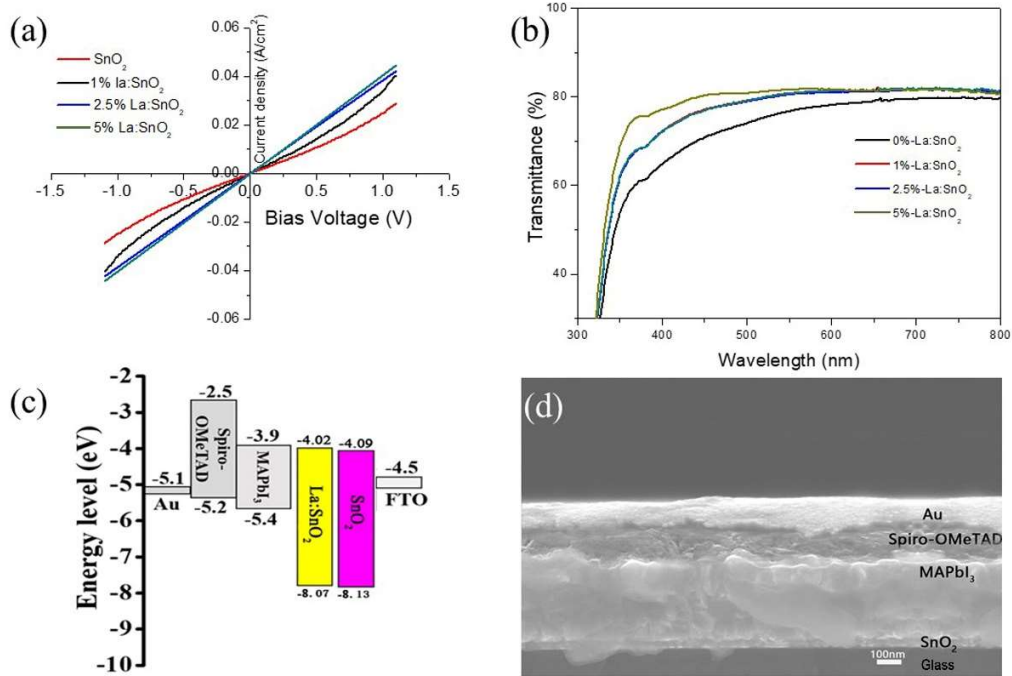

Figure 2. (a) J-V curve of pristine SnO$_2$ and La:SnO$_2$ layers with La contents 1%, 2.5%, and 5%, respectively. (b) Transmittance spectra of pristine SnO$_2$ and La:SnO$_2$ films with different La contents. (c) The energy level diagram of PSCs. (d) Cross-sectional SEM of the device on La:SnO$_2$ ETL.

The top view morphological images of SnO$_2$ and La:SnO$_2$ are shown in Figure 3. The pristine SnO$_2$ (Figure 3a) growth on the FTO was aggregated with the formation of pinholes (red-circled), while a pinhole-free morphological surface of SnO$_2$ (Figures 3b and c) was observed upon the incorporation of a minute amount of La within the SnO$_2$ lattice. It is hypothesized that the pinholes and aggregated island surface could cause severe recombination at the interface between the ETLs and perovskite layer, which is a disadvantage for PSC applications. However, when the dopant concentration is further increased, the morphological surface of the 5%

La:SnO$_2$ with pinholes was again revealed, which implies optimizing the concentration of La is indeed important for the best PSC performances. Clearly, lanthanide doping effectively enhances the SnO$_2$ film coverage quality, reduces the surface-state traps, thus leading to a high photo-generated electron collection ability. Figures 3e and d show the top-view SEM images of the perovskite film deposited on the untreated SnO$_2$ and La:SnO$_2$ ETL. The perovskite film exhibits a uniform crystal size of ca. 400 nm along with a smooth coverage surface coverage. The top SEM of the perovskite layer also reveals the presence of small crystals. It suggests that this tiny crystal at the grain boundary is PbI$_2$ in accordance with the XRD results. The PbI$_2$ is beneficial to decrease the grain boundary, thus suppress the hole (H$^+$) and electron (e$^-$) recombination at the interface and consequently improve the Jsc of the device [44]. Through morphology comparison, there is no obvious changes on the crystal size of MAPbI$_3$ either growth on the SnO$_2$ and La:SnO$_2$-based ETLs. The crystal size of MAPbI$_3$ has no obvious change in the SnO$_2$ and La:SnO$_2$-based ETLs.
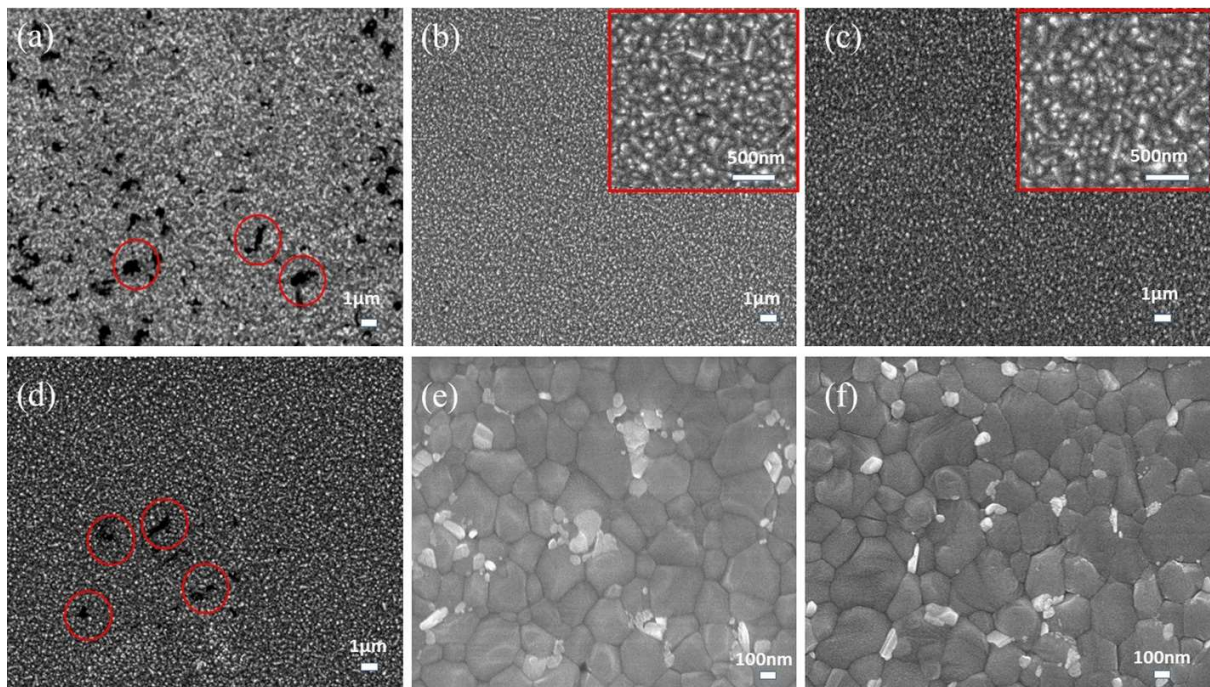
Figure 3. (a), (b), (c), and (d) SEM images of SnO_2, 1% La:SnO_2, 2.5% La:SnO_2 and 5% La:SnO_2 layer, respectively. (e) and (f) SEM of perovskite crystal growth on the pristine SnO_2 and La:SnO_2 ETLs.

The previously mentioned changes show that the SnO_2 film is significantly improved upon the doping of lanthanide. The stable La:SnO_2 layer supported a PSC device with an improved efficiency. Figure 4a reveals the XRD pattern of the perovskite coated on the pristine SnO_2 and La:SnO_2. Both of the peaks (blue and black) are identical to that previously reported. The detail information of the internal crystal strain and crystallite size are fitted by the Williamson-Hall equation (Equation S2). The Williamson-Hall plot is commonly used to reveal trends in the crystallite size and strain, which in turns reveals the properties change of the product. As shown in Figure 4b, the slope of the plot response to the strain and the intercept is related to the inverse crystalline size. The strain of the perovskite is hypothesized to be relaxed on the La:SnO_2 layer with a reduced density of crystal defects. The fitted crystalline size of the La:SnO_2 perovskite is consistent with the SEM results.
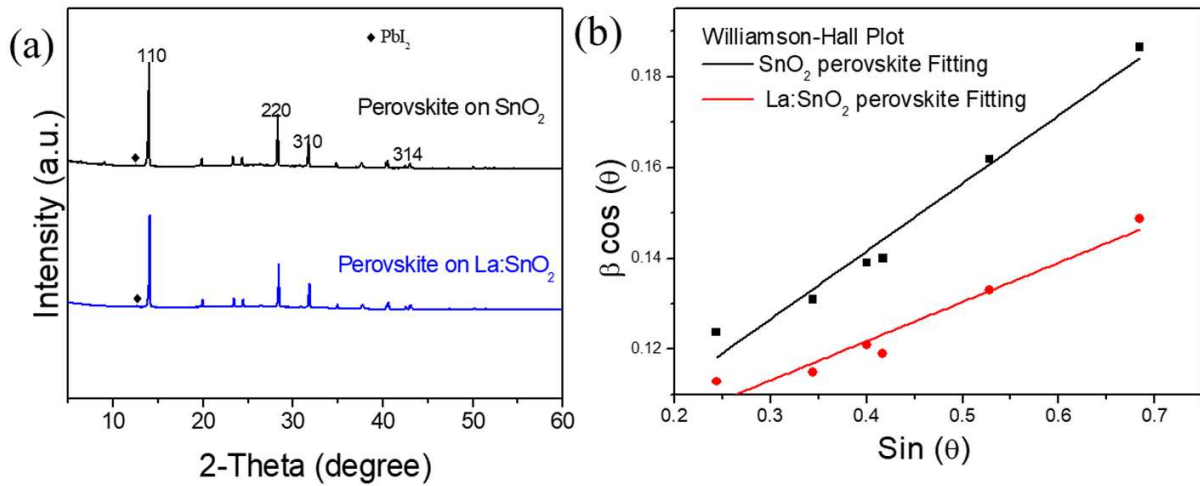
Figure 4. (a) XRD pattern of perovskite on SnO_2 and $La:SnO_2$ (2.5% mol ratio) ETLs respectively. (b) Williamson-Hall fitting of perovskite layer on SnO_2 and $La:SnO_2$ layers.

3.2. Photovoltaic Performance

The photovoltaic performances of the $La:SnO_2$-based PSCs were provided in Figure 5a and Table S2. When the lanthanide doping molar ratio was increased to the optimum concentration of 2.5%, the PCE was substantially increased to 17.08% from 14.24% (for pristine SnO_2). However, further increasing of the La concentration (5%) does not improve the PCE, conversely, the PCE dropped to 15.92%. The pristine SnO_2 ETL gives a PCE of 14.24% with Jsc of 20.67 mA·cm^{-2}, V_{OC} of 1.06 V, and FF of 0.65 from a reverse scan direction. When La is doped into the SnO_2 ETL, the PCE rapidly increased to 17.08% with the Jsc of 21.77 mA·cm^{-2}, V_{OC} of 1.09 V, and FF of 0.72. The enhanced J_{SC} and FF are due to the higher electron conductivity and reduced resistance of the $La:SnO_2$ ETL. The increased V_{OC} is ascribed to the upshifted conduction band level of $La:SnO_2$ which is perfectly matched to the perovskite layer. Figure 5b shows the IPCE and integrated current based on the various ETLs. The IPCE integrated current density for the SnO_2-based cell is 19.31mA·cm^{-2}, and it increased to 21.07 mA·cm^{-2} for the device on the $La:SnO_2$ layer, which is in accordance with the J-V measurement values. The EIS plot of the devices on the pristine SnO_2 and $La:SnO_2$ ETLs are shown in Figure S4d where the series resistance (Rs), which corresponds to fitting R1, decreased from 4.92Ω to 1.12Ω, implying an efficient injection and transfer of electrons at the $La:SnO_2$/perovskite interface.
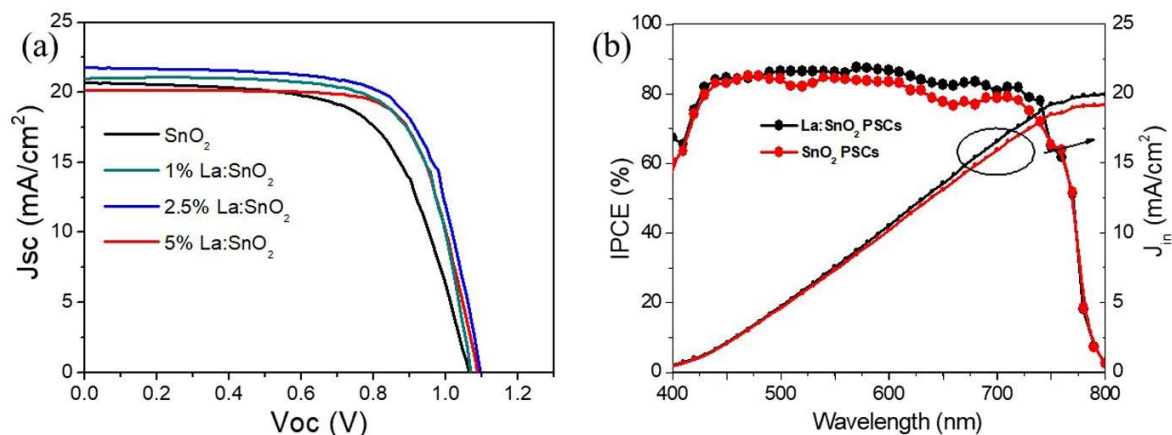
Figure 5. (a) The J−V curves of PSCs devices based on pristine SnO_2 and $La:SnO_2$ with different La doping contents. (b) IPCE of the PSCs based on SnO_2 and $La:SnO_2$ ETLs, respectively.

The stability and reproducibility of the device were studied by preparing more than 20 individual devices based on the SnO_2 and $La:SnO_2$ ETLs without encapsulation. Figure S3 presents the distribution of the PCE, Voc, and Jsc with the statistics summarized in Table S3. During the measurements, the cells were kept under light coverage at a humidity of ca. 70%. For the $La:SnO_2$-based PSC, the PCE of the cells could still retain 74% of its initial efficiency after 10 days of storage, while only 45% of its initial efficiency was retained for the SnO_2-based device. The improved stability performance could be due to the alleviated hysteresis effect (4.5%) of the $La:SnO_2$ relative to the high hysteresis of the pristine SnO_2 layer (5.5%). The steady state output (Figure S4) at the maximum power point of the PSCs was carried out, in which there was no obvious decrease in the current after a 30-min constant illumination.
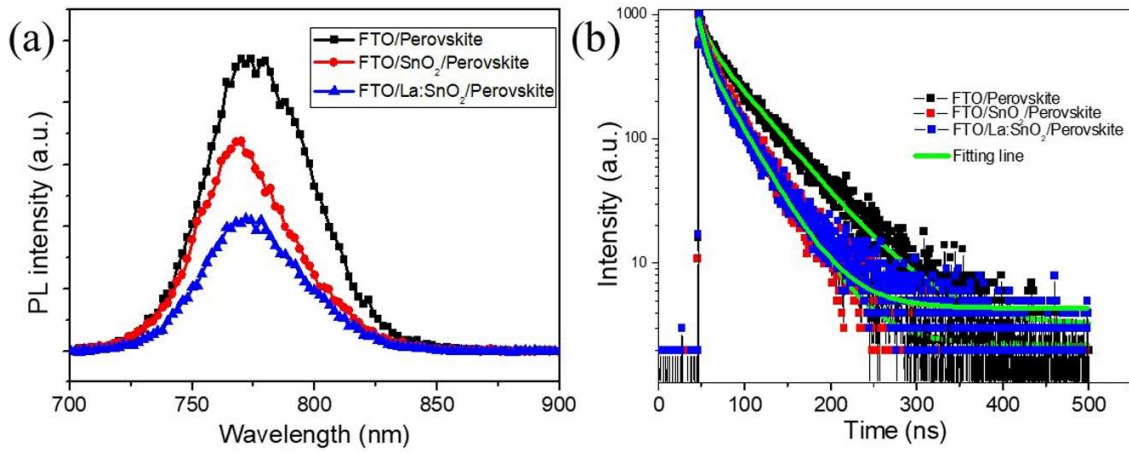
Figure 6. (a) Steady-state photoluminescence (PL) spectra of the FTO/perovskite, FTO/SnO$_2$/perovskite, and FTO/La:SnO$_2$/perovskite samples. (b) Time-resolved photoluminescence (TRPL) of perovskite absorber deposited on SnO$_2$ and La:SnO$_2$ substrates.

To investigate the electron extraction and transport mechanism of the device, the steady-state PL and TRPL were measured for the perovskite layer on the SnO$_2$ and La:SnO$_2$ layers, respectively. As shown in Figure 6a, the PL spectra of the FTO/perovskite apparently exhibited the highest PL intensity, indicating a serious recombination in the cell. The FTO/La:SnO$_2$/ perovskite sample with reduced recombination, led to a more effective electron extraction ability. Figure 6b displays the TRPL spectra of the same devices. The PL decay time and amplitudes are fitted using the exponential ExpDecay 2 (Equation S3) and the fitting results are listed in Table 1. Commonly, the fast component (τ_1) in the PL decay is expected to indicate the presence of defect trapping, and the slow component (τ_2) is responsible for the recombination lifetime. The average decay time of the FTO/SnO$_2$/perovskite is 41.05 ns, and it reduces to 27.33 ns for the device on La:SnO$_2$. This indicated that the electron transport is faster from the perovskite layer into the La:SnO$_2$ ETL. The rapid charge injection rate from the perovskite layer to La:SnO$_2$ ETL is beneficial to

the electron-hole separation and effectively suppressed the charge recombination at the interface, resulting in higher Jsc and FF values.

Table 1. A fitting summary of the TRPL Spectroscopy based on the FTO/Perovskite, FTO/SnO$_2$/Perovskite, and FTO/La:SnO$_2$/Perovskite, respectively

Samples	τ_{ave} (ns)	τ_1 (ns)	Amplitude τ_1 (%)	τ_2 (ns)	Amplitude τ_2 (%)
FTO/perovskite	671.62	51.01	65.01	750.23	34.99
FTO/SnO$_2$/perovskite	41.05	10.21	67.44	35.17	32.56
FTO/La:SnO$_2$/perovskite	27.33	6.4	67.11	35.12	32.89

4. Conclusions

In summary, La:SnO$_2$ as an effective ETL in PSCs has been successfully prepared by a low temperature processing at 180 °C. We found that the addition of lanthanide to the tin precursor solution can reduce the SnO$_2$ crystal aggregation, resulting in a pinhole-free surface morphology. The conductivity and transparency of the SnO$_2$ were enhanced after the lanthanide addition, thus facilitated the charger injection and transfer of electrons. Furthermore, the upshift of the CBM reduces the band offset at the La:SnO$_2$/perovskite interface, thus minimizing the energy loss leading to a Voc up to 1.11 V. This study revealed the advantages of lanthanide doping within the SnO$_2$ layer, which is an important approach for improving the performance of PSCs with a low-temperature processed ETL fabrication.

Appendix A. Supplementary data

The detail of Debye-Hückel simplified equation, Williamson-Hall equation, and simulation equation ExpDecay 2. PYS pattern of La:SnO2 layer and the bandgap calculation. Summary parameters and distribution of PSCs device on different SnO_2 ETLs. EIS spectrum of the device.

References

[1] S. Kurtz, N. Haegel, R. Sinton, and R. Margolis, A new era for solar, Nature Photonics 11 (2017) 3-5.

[2] N. J. Jeon, J. H. Noh, Y. C. Kim, Yang W. S., Ryu S., and S. I. Seok, Solvent engineering for high-performance inorganic-organic hybrid perovskite solar cells, Nature materials 13 (**2014**) 897-903.

[3] M. Saliba, T. Matsui, J. Y. Seo, K. Domanski, J. P. Correa-Baena, M. K. Nazeeruddin, M. Gratzel, Cesium-containing triple cation perovskite solar cells: improved stability, reproducibility and high efficiency, Energy & Environmental Science 9 (2016) 1989-1997.

[4] V. Gonzalez-Pedro, E. J. Juarez-Perez, W. S. Arsyad, E. M. Barea, F. Fabregat-Santiago, I. Mora-Sero, and J. Bisquert, General working principles of $CH_3NH_3PbX_3$ perovskite solar cells, Nano Letters 14 (2014) 888-893.

[5] Q. Jiang, X. Zhang, J. You, SnO_2: A Wonderful Electron Transport Layer for Perovskite Solar Cells, Small 2 (2018) 1801154.

[6] Q. Dong, Y. Shi, K. Wang, Y. Li, S. Wang, H. Zhang, Y. Xing, Y. Du, X. Bai, T. Ma, Insight into Perovskite Solar Cells Based on SnO_2 Compact Electron Selective Layer, J. Phys. Chem. C 119 (2015) 10212-10217.

[7] E. Calabrò, F. Matteucci, A. L. Palma, L. Vesce, B. Taheri, L. Carlini, S. Nappinic, J. Dagara, C. Battocchio, T. M. Brown, A. D. Carlo, Low temperature solution-processed perovskite solar cells and modules with an aperture area efficiency of 11%, Solar Energy Materials and Solar Cell 185 (2018) 136–144.

[8] Q. Jiang, L. Zhang, H. Wang, X. Yang, J. Meng, H. Liu, Z. Yin, J. Wu, X. Zhang, J. You, Enhanced electron extraction using SnO_2 for high-efficiency planar-structure $HC(NH_2)_2PbI_3$-based perovskite solar cells, Nature Energy 2 (2016) 16177.

[9] G. Yang, C. Chen, F. Yao, Z. Chen, Q. Zhang, X. Zheng, J. Ma, H. Lei, P. Qin, L. Xiong, W. Ke, G. Li, Y. Yan, G. Fang, Effective Carrier-Concentration Tuning of SnO_2 Quantum Dot Electron-Selective Layers for High-Performance Planar Perovskite Solar Cells, Adv. Mater 26 (2018) 1706023.

[10] W. Ke, G. Fang, Q. Liu, L. Xiong, P. Qin, H., J. Wang, H. Lei, B. Li, J. Wan, G. Yang, and Y. Yan, Low-Temperature Solution-Processed Tin Oxide as an Alternative Electron Transporting Layer for Efficient Perovskite Solar Cells, J. Am. Chem. Soc. 137 (2015) 6730−6733.

[11] L. Xiong, Y. Guo, J. Wen, H. Liu, G. Yang, P. Qin, G. Fang, Review on the Application of SnO_2 in Perovskite Solar Cells, Adv. Funct. Mater. 2 (2018) 1802757.

[12] P. Zhao, B. J. Kim, H. S. Jung, Passivation in perovskite solar cells: A review, Materials Today Energy 7 (2018) 267-286.

[13] C. Xiao, C. Wang, W. Ke, W. P. Gorman, J. Ye, C. Jiang, Y. Yan, M. A. Mowafak, Junction Quality of SnO_2 Based Perovskite Solar Cells Investigated by Nanometer-Scale Electrical Potential Profiling, ACS Applied Materials & Interfaces 9 (2017) 38373-38380.

[14] Laboratory, N. R. E. L. Best Research-Cell Efficiencies. http://www.nrel.gov/pv/assets/images/efficiency_chart-20180716.jpg.

[15] D. Yang, R. Yang, K. Wang, C. Wu, X. Zhu, J. Feng, X. Ren, G. Fang, S. Priya, S. Liu, High efficiency planar-type perovskite solar cells with negligible hysteresis using EDTA-complexed SnO_2, Natural comm. 9 (2018) 3239.

[16] Y. Lee, S. Paek, K. T. Cho, E. Oveisi, P. Gao, S. Lee, J. Park, Y. Zhang, R. H. Baker, A. M. Asirid and M. K. Nazeeruddin, Enhanced charge collection with passivation of the tin oxide layer in planar perovskite solar cells. J. Mater. Chem. A, 2017, 5, 12729-12734.

[17] Y. Wang, C. Duan, J. Li, W. Han, M. Zhao, L. Yao, Y. Wang, C. Yan, T. Jiu, Performance Enhancement of Inverted Perovskite Solar Cells Based on Smooth and Compact $PC_{61}BM:SnO_2$ Electron Transport Layers, ACS Appl. Mater. Interfaces 10 (2018) 20128-20135.

[18] Z. Liu, B. Sun, X. Liu, J. Han, H. Ye, Y. Tu, C. Chen, S. Shi, Z. Tang, G. Liao, 15% efficient carbon based planar-heterojunction perovskite solar cells using a TiO_2/SnO_2 bilayer as the electron transport layer, J. Mater. Chem. A 6 (2018) 7409-7419.

[19] D. Wang, C. Wu, W. Luo, X. Guo, B. Qu, L. Xiao, Z. Chen, ZnO/SnO_2 Double Electron Transport Layer Guides Improved Open Circuit Voltage for Highly Efficient $CH_3NH_3PbI_3$-Based Planar Perovskite Solar Cells, ACS Appl. Energy Mater. 1 (2018) 2215-2221.

[20] J. Dagar, S. Castro, H. Matteo, L. G. Alessandro, L. Cina, F. Matteucci, E. Calabrò, A. D. Carlo, T. M. Brown, Efficient fully laser-patterned flexible perovskite modules and solar cells based on low-temperature solution-processed SnO_2/mesoporous-TiO_2 electron transport layers, Nano Research 11 (2018) 2669–2681.

[21] M. M. Tavakoli, F. Giordano, S.M. Zakeeruddin, M. Gratzel, Mesoscopic Oxide Double Layer as Electron Specific Contact for Highly Efficient and UV Stable Perovskite Photovoltaics, Nano Lett. 18 (2018) 2428–2434.

[22] S. Song, G. Kang, L. Pyeon, C. Lim, G. Lee, T. Park, J. Choi, Systematically Optimized Bilayered Electron Transport Layer for Highly Efficient Planar Perovskite Solar Cells ($\eta = 21.1\%$), ACS Energy Lett. 2 (2017) 2667–2673.

[23] J. Xie, K. Huang, X. Yu, Z. Yang, K. Xiao, Y. Qiang, X. Zhu, L. Xu, P. Wang, C. Cui, D. Yang, Enhanced Electronic Properties of SnO_2 via Electron Transfer from Graphene Quantum Dots for Efficient Perovskite Solar Cells, ACS Nano. 11 (2017) 9176–9182.

[24] X. Zhao, L. Tao, H. Li, W. Huang, P. Sun, J. Liu, S. Liu, Q. Sun, Z. Cui, L. Sun, Y. Shen, Y. Yang, M. Wang, Efficient Planar Perovskite Solar Cells with Improved Fill Factor via Interface Engineering with Graphene, Nano Lett. 18 (2018) 2442–2449.

[25] Y. Wang, X. Zhang, Q. Jiang, H. Liu, D. Wang, J. Meng, J. You, Z. Yin, Interface Engineering of High-Performance Perovskite Photodetectors Based on PVP/SnO$_2$ Electron Transport Layer, ACS Appl. Mater. Interfaces 10 (2018) 6505–6512.

[26] C. Huang, P. Lin, N. Fu, K. Sun, M. Ye, C. Liu, X. Zhou, L. Shu, X. Hao, B. Xu, Z. Zeng, Y. Wang, S. Ke, Ionic Liquid Modified SnO$_2$ Nanocrystals as the Robust Electron Transporting Layer for Efficient Planar Perovskite Solar Cells, J. Mater. Chem. A (2018) DOI: 10.1039/C8TA04131H.

[27] X. Zeng, T. Zhou, C. Leng, Z. Zang, M Wang, W. Hu, X. Tang, S. Lu, L. Fang and M. Zhou., Performance improvement of perovskite solar cells by employing a CdSe quantum dot/PCBM composite as an electron transport layer. J. Mater. Chem. A 2017, 5, 17499-17505.

[28] Y. Lee, S. Paek, K. T. Cho, E. Oveisi, P. Gao, S. Lee, J. Park, Y. Zhang, R. H. Baker, A. M. Asirid, M.K. Nazeeruddin, Enhanced charge collection with passivation of the tin oxide layer in planar perovskite solar cells. J. Mater. Chem. A 5 (2017) 12729-127340.

[29] P. Wang, L. Zhao, J. Liu, L. Wei, Z. Liu, L. Guan, G. Cao, Stabilization of organometal halide perovskite films by SnO$_2$ coating with inactive surface hydroxyl groups on ZnO nanorods, Journal of Power Sources 339 (2017) 51-60.

[30] M. Park, J. Kim, H. J. Son, C. Lee, S. S. Jang, M. J. Koa, Low-temperature solution-processed Li-doped SnO$_2$ as an effective electron transporting layer for high-performance flexible and wearable perovskite solar cells, Nano Energy 26 (2016) 208-215.

[31] H. Chen, D. Liu, Y. Wang, C. Wang, T. Zhang, P. Zhang, H. Sarvari, Z. Chen, S. Li, Enhanced Performance of Planar Perovskite Solar Cells Using Low-Temperature Solution-Processed Al-Doped SnO$_2$ as Electron Transport Layers, Nanoscale Research Letters 12 (2017) 238.

[32] L. Xiong, M. Qin, C. Chen, J. Wen, G. Yang, Y. Guo, J. Ma, Q. Zhang, P. Qin, S. Li, G. Fang, Fully High-Temperature-Processed SnO$_2$ as Blocking Layer and Scaffold for Efficient, Stable, and Hysteresis-Free Mesoporous Perovskite Solar Cells, Adv. Funct. Mater. 28 (2018) 1706276.

[33] X. Liu, Y. Zhang, L. Shi, Z. Liu, J. Huang, J. S. Yun, Y. Zeng, A. Pu, K. Sun, Z. Hameiri, J. A. Stride, J. Seidel, M. A. Green, X. Hao, Exploring Inorganic Binary Alkaline Halide to Passivate Defects in Low-Temperature-Processed Planar-Structure Hybrid Perovskite Solar Cells, Adv. Energy Mater. 28 (2018) 1800138.

[34] E. H. Anaraki, A. Kermanpur, M. T. Mayer, L. Steier, T. Ahmed, T. Cruz, J. Seo, J. Luo, S. M. Zakeeruddin, W. R. Tress, T. Edvinsson, M. Gratzel, A. Hagfeldt, C. Baena, Low-Temperature Nb-Doped SnO_2 Electron Selective Contact Yields over 20% Efficiency in Planar Perovskite Solar Cells, *ACS Energy Lett. 3 (***2018**) 773-778.

[35] X. Ren, D. Yang, Z. Yang, J. Feng, X. Zhu, J. Niu, X. Liu, W. Zhao, S. Liu, Solution-Processed $Nb:SnO_2$ Electron Transport Layer for Efficient Planar Perovskite Solar Cells, ACS Appl. Mater. Interfaces 9 (2017) 2421-2429.

[36] X. Gong, Q. Sun, S. Liu, P. Liao, Y. Shen, C. Graetzel, S. M. Zakeeruddin, M. Gratzel, M. Wang, Highly Efficient Perovskite Solar Cells with Gradient Bilayer Electron Transport Materials, Nano Lett. 18 (2018) 3969-3977.

[37] J. Khan, Y. Yang, K. Qiao, H. Deng, J. Zhang, Z. Liu, W. Ahmad, J. Zhang, D. Li, H. Liu, H. Song, C. Cheng, J. Tang, Low-temperature-processed SnO_2–Cl for efficient PbS quantum-dot solar cells via defect passivation, J. Mater. Chem. A 5 (2017) 17240-17247.

[38] P. Wang, J. Wang, X. Zhang, H. Wang, X. Cui, S. Yuan, H. Lu, L. Tu, Y. Zhan, L. Zheng, Boosting performance of perovskite solar cells through a novel active passivation method. J. Mater, Chem. A 6 (2018) 15853-15858.

[39] Z. Guo, L. Gao, C. Zhang, Z. Xu, T. Ma, Low-temperature processed non-TiO_2 electron selective layers for perovskite solar cells, *J. Mater. Chem. A* 6 (2018) 4572-4589.

[40] S. S. Shin, E. J. Yeom, W. S. Yang, S. Hur, M.J. Kim, J. Im, J. Seo, J. H. Noh, S. Seok, Colloidal prepared La-doped $BaSnO_3$ electrodes for efficient, photostable perovskite solar cells, Science 356 (2017) 167–171.

[41] X. Gao, Q. Ge, D. Xue, J. Ding, J. Ma, Y. Chen, B. Zhang, Y. Feng, L. Wan J., Hu, Tuning the Fermi-Level of TiO_2 Mesoporous Layer by Lanthanum Doping towards Efficient Perovskite Solar Cells, Nanoscale 8 (2016) 16881-16885.

[42] H. Sun, K. Deng, Y. Zhu, M. Liao, J. Xiong, Y. Li, L. Li, A Novel Conductive Mesoporous Layer with a Dynamic Two-Step Deposition Strategy Boosts Efficiency of Perovskite Solar Cells to 20%, Adv. Mater.28 (2018) 1801935.

[43] H. Wong, H. Iwai, K. Kakushim, B. L. Yang, B. L. Chu, XPS Study of the Bonding Properties of Lanthanum Oxide/Silicon Interface with a Trace Amount of Nitrogen Incorporation, J. Electrochem. Soc. 157 (2010) 49-52.

[44] W. Ke, C. Xiao, C. Wang, B. Saparov, H. Duan, D. Zhao, Z. Xiao, P. Schulz, S.P. H, W. Liao, W. Meng, Y. Yu, A. J. Cimaroli, C. Jiang, K. Zhu, M. Al-Jassim, G. Fang, D. B. Mitzi, Y. Yan, Employing Lead Thiocyanate Additive to Reduce the Hysteresis and Boost the Fill Factor of Planar Perovskite Solar Cells, Adv. Mater. (28) 2016 5214-5221.